Investigation of Temperature-Driven Water Transport in Polymer Electrolyte Fuel Cell: Phase-Change-Induced Flow

Soowhan Kim* and M. M. Mench**,z

Fuel Cell Dynamics and Diagnostics Laboratory, Department of Mechanical and Nuclear Engineering, The Pennsylvania State University, University Park, Pennsylvania 16802, USA

The objective of this work is to investigate phase-change-induced water transport of polymer electrolyte fuel cell materials subjected to a temperature gradient. Contrary to thermo-osmotic flow in fuel cell membranes, a net flux of water was found to flow from the hot to the cold side of the full membrane electrode assembly. The key to this is the existence of some gas phase in the catalyst layer or other porous media. This mode of transport is a result of phase-change-induced flow. The measured water transport through the membrane electrode assembly is the net effect of mass diffusion as well as thermo-osmosis in the membrane, which moves counter to the direction of the phase-change-induced flow. Arrhenius functions that are dependent on material set, temperature gradient, and average temperature across the materials were developed that describe the net flux. In addition to direct quantification, phase-change-induced flow was visualized and confirmed using high-resolution neutron radiography.

© 2009 The Electrochemical Society.   [DOI: 10.1149/1.3046136] All rights reserved.

Proper water management is critical to achieve high performance and durability for polymer electrolyte fuel cells (PEFCs). The most commonly used polymer electrolyte membranes (PEMs) require hydration for acceptable protonic conductivity, but liquid water in the catalyst layers (CLs), diffusion media (DM), channels, and along the various interfaces can cause performance loss resulting from restriction of reactant transport to the catalysts, a phenomenon generically known as flooding. The fuel cell should also be capable of damage-free start-up from frozen conditions. Excessive residual liquid water contact with the CL at shutdown to freezing conditions has been shown to cause irreversible damage[1,2] and reduces cold start capability by occupying CL pore volume. Thus, to optimize operational performance and extend the operational lifetime, water transport modes in the membranes as well as porous media (CL and DM) should be well understood.

Water transport by electro-osmotic drag, diffusion, and hydraulic permeation in the PEMs has been well explored.[3-11] Capillary and diffusion water transport in the DM has also been well studied.[12-15] However, temperature-gradient-driven water transport modes, thermo-osmosis in the membrane and phase-change-induced flow (also known as heat pipe effect, although this is technically not a heat pipe) in the porous media are not yet well explored. Temperature-gradient-driven water flow is potentially attractive because of the possibility of tailoring material properties or stack design to avoid flooding or for nonparasitic water drainage during shutdown using naturally occurring temperature gradients within the stack.[16-18]

Under fuel cell operation, a temperature difference can occur in the thru-plane direction depending on operating conditions, such as at high current.[19] At 1 A/cm² current density, the interfacial temperature of the membrane in contact with cathode CLs can be >1°C higher than that of the bulk membrane, and an even higher difference can occur across the DM.[16,17] Weber and Newman[17] and Wang and Wang[20] showed, in their nonisothermal models, that water transport mode by evaporation in the porous media (evaporation in the CLs and condensation in the DM or flow-field plates) plays an important role in high current and elevated temperature regimes. Hickner et al.[21-23] observed the importance of evaporative water transport in the higher current region.

As a first approximation, temperature-driven flow in the porous media (phase-change-induced flow) can be treated as a gas-phase diffusion process induced by a thermodynamic saturation pressure gradient. However, temperature-driven flow in the membrane (thermo-osmosis) is a fundamentally different transport mode. When a membrane separates liquid water at different temperatures, water flows from the hot to cold direction or vice versa, a process known as thermo-osmosis. The direction of water flow depends on the entropy difference between water in the membrane and external to the membrane; for example, water in a hydrophilic membrane can be considered to have a relatively ordered state compared to water existing outside the membrane. Therefore, unbound water transport from the cold to the hot side leads to an increase of total entropy and is thus thermodynamically favored.[24] For hydrophobic membranes, water typically flows from the hot to cold direction, based on a similar entropy-based argument.[24,25] Despite this established conventional understanding, incomplete understanding on the direction and magnitude of water flux for different fuel cell materials and combinations of materials still exists, as summarized in Table I.

Kim and Mench[26,27] observed that thermo-osmotic flux of water in three different commercial perfluorinated PEMs flows from the cold to hot side of the membrane and that reinforcement did not affect the flow direction. The net flux, however, was altered by the reinforcement structure. The water flux was higher in membranes with lower equivalent weight (EW) and decreased thickness. The water flux was proportional to temperature gradient and showed Arrhenius behavior with average temperature dependency, which agrees with literature.[25,28] Results indicated that the thermo-osmotic water flux has a similar order of magnitude to mass diffusion flux and should not be neglected under high current or start-up/shutdown operation. Empirical thermo-osmotic water flux relations were presented, which can be used by modelers and design engineers.

Villaluenga et al.[28] observed that water flows from the cold to hot side in the Nafion 117 membrane, which agrees with Tasaka et al.'s[25] observation in Nafion 417. Water flux was proportional to temperature difference and increased with average membrane temperature. The temperature dependency of water flux showed Arrhenius behavior for Villaluenga et al.[28] However, Zaffou et al.[29,30] observed that there was hot to cold thermo-osmotic flow in the polytetrafluoroethylene (PTFE)-reinforced membrane, but did not observe thermo-osmosis in the nonreinforced Nafion membranes. Bradean et al.[18] and Perry et al.[31,32] observed net water flux from the hot to the cold side in complete membrane electrode assemblies (MEAs) with DM in a real fuel cell stack. (In this work, we refer to MEA as a three-layer CL-membrane-CL structure.) It should be noted that Villaluega et al.[28] and Tasaka et al.[24,25] used bare membranes, but Zaffou et al.[29,30] used fuel cell fixtures where the membrane was sandwiched between highly porous DM.

Temperature-driven flow during fuel cell operation, as well as at shutdown, can be important, but is still not completely understood. Kim and Mench[26,27] observed net water flux reversal in membranes when hydrophilic DM were replaced with hydrophobic DM. With fully saturated hydrophilic DM and membranes, the net flow was thermo-osmosis through the membrane from the cold to the hot side.

Table I. Summary of published studies of temperature gradient-driven flow in PEFCs.

Ref.	Materials	Observations
26 and 27	Nafion 112 Commercial reinforced perfluorinated membranes	$J = 3.3 \times 10^{-4}$ kg/m^2 s at $T_{avg} = 65°C$, $\Delta T = 0.3°C$ for commercial reinforced membrane (18 μm thickness) Similar order of magnitude to mass diffusion Empirical thermo-osmosis flux relations Water flows from cold to hot side
28	Nafion 117 ($t = 183$ μm, EW = 1100)	$J = 7.5 \times 10^{-6}$ kg/m^2 s at $T_{avg} = 26.5°C$, $\Delta T_b = 10°C$ Water flows from cold to hot side
25	Nafion 417 ($t = 430$ μm, EW = 1613)	$J = 3.6 \times 10^{-5}$ kg/m^2 s at $T_{avg} = 35°C$, $\Delta T = 10°C$ Water flows from cold to hot side
29 and 30	Nafion 112 ($t = 51$ μm, EW = 1100)	No water flow
	PTFE-reinforced Nafion 112	$J = 4.1 \times 10^{-4}$ kg/m^2 s at $T_{avg} = 65°C$, $\Delta T = 1°C$ Water flows from hot to cold side
	Catalyst-coated Nafion 112	No water flow
	Catalyst-coated Gore-Select (5510 MEA)	$J = 6.9 \times 10^{-4}$ kg/m^2 s at $T_{avg} = 65°C$, $\Delta T = 1°C$ Water flows from hot to cold side
18	MEA (20 cell stack)	$J = 3.0 \times 10^{-6}$ kg/m^2 s during cooling [66 $\rightarrow$ ~ 33°C (3 h)] Water flows from hot to cold side
31 and 32	MEA (30 cell stack)	Water flows from hot to cold side Freeze-damage of anode end cell

When hydrophobic DM or a CL was used with the membrane, the net flux under an imposed temperature gradient was reversed from the hot to the cold side, even with fully liquid-filled flow channels. Clearly, the existence of some gas-phase plays a key role in determining the net direction of water flux direction.

Contradictions regarding the net flow direction presented in the literature may come from the fact that fuel cell consists of materials with different hydrophobicity. Hydrophobicity prevents complete liquid-phase saturation in the porous media (DM and CL), allowing vapor diffusion across a temperature gradient. Vapor diffusion always results in flow from higher saturation pressure (high temperature) to lower saturation pressure (low temperature), but thermo-osmotic water transport in a perfluorinated membrane flows from the cold to the hot side.[25-28]

Thus, the temperature-gradient-induced water transport in the fuel cell should be considered to be the net flux of phase-change-induced flow in porous media and thermo-osmosis in the membrane. We also expect that the phase-change-induced flow would be more dominant with increasing temperature because the saturation pressure is a highly nonlinear function of temperature.

Some inclusion of water transport in the DM by the phase-change-induced flow based solely on thermodynamics has been implemented in nonisothermal models,[17,20] but temperature-driven flow in an individual fuel cell has not been definitively explored experimentally or numerically validated. This work is motivated by the need to understand and quantify water transport driven by temperature gradient in the fuel cell materials. Using an in-house fuel cell, phase-change-induced flow was carefully quantified as a function of materials, average cell temperature, and temperature gradient. Water transport behavior under temperature gradient was also confirmed and visualized using high-resolution neutron radiography at the National Institute of Standards and Technology (NIST).

Method of Approach

The impact of hydrophobicity on water transport under a temperature gradient in fuel cell materials was explored using direct measurement of water flux as well as visualization by neutron radiography.

Direct measurement of water flux.— The test cell utilized was designed for direct measurement of water flux driven by temperature gradient, as well as for fuel cell testing (Fig. 1). The test

setup consisted of two precisely temperature-controlled (accuracy $\pm$ 0.01°C) refrigerated circulators (VWR International, USA, model no. 1196D), the test fuel cell, a distilled water reservoir, a vacuum pump, nine T-type thermocouples, nine manual valves, and calibrated perfluoroalkoxy (PFA) tubing (Swagelok, tube size 0.25 in. and wall thickness 0.062 in.). For precise temperature difference uniformity two separate coolant streams were circulated through the test cell coolant plates at maximum flow rate (22 L/min) in the counterflow direction. Three temperature sensors were inserted in the middle of each flow-field plate, located at the inlet, center, and outlet positions with respect to the flow direction. These thermocouples (not shown in Fig. 1) were used to control circulator temperatures, enabling proper boundary condition control. Two thermocouples (TC11 and TC21) were inserted in the T-junction of PFA tubing to monitor water temperature inside the tube. The other temperature sensor measured the ambient temperature. The valves and vacuum pump were used to fill water inside the test cell and remove air pockets. For example, after maintaining the test cell below −750 mmHg with valves V12 and V22 opened and other valves closed, both sides of the test cell were filled by opening
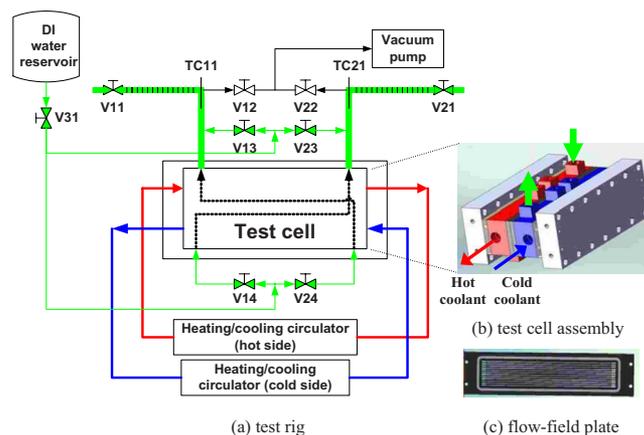

Figure 1. (Color online) Schematic of test cell to measure water transport driven by temperature gradient in PEFCs.

Table II. Summary of materials used in this work.

	Membranes/MEA Combinations		DM
Membrane	Nafion 112	EW = 1100, t = 51 μm	SGL 10BB
	Gore-Select membrane (R-PEM)	EW < 1000,[33] t = 18 μm	SGL 10BB
MEA	Gore-Primea 5710 series MEA (R-MEA)	Pt 0.4 mg/cm²-electrode Gore-Select 18 μm thick membrane	SGL 10AA SGL 10BA SGL 10BB
	NR-MEA	Pt 0.4 mg/cm²-electrode Nonreinforced 18 μm thick membrane	

SGL10AA:[34] no PTFE content, 390 μm thickness, 88% porosity
SGL10BA:[34] 5% PTFE. 400 μm thickness, 88% porosity
SGL10BB:[34] 5% PTFE, MPL (23% PTFE + carbon black), 420 μm thickness

valves V14, V24, and V31. After the temperature of the flow-field plates reached the desired experimental temperatures, the water inside the tube was flushed using valve operations (open V31, V11, V21, V13, and V23, and close the others) to maintain the tube water temperature below 30°C, reducing evaporation loss of water in the PFA tubing to negligible levels. All valves except for V11 and V21 were closed for measurement of water flux.

As shown in Fig. 1b, the test cell consisted of two flow-field plates, two cooling plates, and two end plates. The flow-field plate is machined impregnated fuel cell grade graphite with 12 parallel channels (1 mm width and 0.6 mm depth) and 0.75 mm wide lands. The cell active area is 23.75 cm², with identical anode and cathode flow fields. For sealing, flat fluorine rubber gaskets (width 2 mm and thickness 0.7 mm) were attached on the grooved surface in each flow-field plate. The cooling plate consisted of gold-plated aluminum (thickness 20 mm) and Lexan (thickness 5 mm). The surface with parallel cooling channels (2 mm depth and 3.1 mm width) was bonded by a Lexan plate, serving as a thermal and electrical insulator. The surface temperature of gold-plated aluminum in contact with the flow-field plate was nearly uniform, providing a uniform thermal boundary condition. Stainless steel end plates (thickness 20 mm) were used to provide evenly distributed compression at contact pressures similar to those used in normal fuel cells (e.g., 1–1.5 MPa). To prevent localized overcompression, incompressible PTFE-coated fiberglass shims were inserted in the border area of flow-field plates. A fiberglass washer was also inserted for each bolt, ensuring thermal and electrical isolation.

The water transport rate was calculated by measuring the change of water volume in the cold and hot side calibrated tubes. The water volume in the tube was calibrated by weighing different lengths of water using an accurate balance (resolution 0.001 g). Water transport by hydraulic pressure gradient was negligible because the tubes in the hot and cold sides were configured symmetrically.

The impact of DM hydrophobicity was investigated with Nafion 112 (termed N112) and a commercialized Gore-Select 18 μm thick reinforced membrane (termed R-PEM) using SGL 10BB DM [5% PTFE and microporous layer (MPL)]. The R-PEM has a lower EW than the N112 membrane. The effect of the existence of CLs was explored using a Gore-Primea 5710 series MEA with the same Gore-Select 18 μm thick reinforced membrane (termed R-MEA) and hydrophilic SGL10AA DM (0% PTFE) as well as hydrophobic DM [SGL10BA (5% PTFE) and SGL10BB (5% PTFE and MPL)]. To investigate the effect of membrane reinforcement, an MEA with nonreinforced membrane (termed NR-MEA) was tested. Note that NR-MEA has the identical CLs and EW to R-MEA. The material properties of tested cases are summarized in Table II.

For membrane only test cases, the assembled cell was soaked at 95°C for 9 h prior to measurement, ensuring the membrane was fully saturated and activated. For three-layer MEA cases, the assembled cell was electrochemically activated at 65°C and ambient pressure with fully humidified hydrogen/air by repeated cycling between 0.4 V and open-circuit voltage (OCV) for 2 h. Measurements were conducted with liquid-filled and evacuated flow channels at average cell temperatures of 80, 65, 45, and 30°C with a temperature difference between flow-field plates of 10, 5, and 3°C. Note that for R-MEA with SGL 10BB test case, water flux was measured at the average cell temperature of 85, 65, 45, 25, and 10°C. Each test condition was repeated three times, and the test duration was sufficiently long to minimize the measurement error and assure a steady state had been achieved.

Visualization by neutron radiography.— The water behavior under temperature gradient was visualized using neutron radiography at the NIST, where a small field-of-view (2.5 cm²) high-resolution (~25 μm) neutron imaging system exists. Figure 2 shows the schematic of the test cell, flow-field plates, and visualized zones. The original test cell used in Ref. 23 was modified with external coolant flow-field plates and fed by separate coolant baths to enable temperatures of both flow-field plates to be independently controlled. The same cooling plates and compression end plates used in the direct temperature-driven water flux experiment shown in Fig. 1 were used. An additional temperature-sensing hole was machined in the center of the flow-field plate, away from the contact surface with DM. The flow-field plate has a single serpentine channel (1 mm width and 1 mm depth) with 1 mm land and has the identical design in both the anode and cathode. The details of high-resolution radiography on the unmodified test cell are described in the literature.[23]

The tested materials were R-MEAs with SGL 10AA (0% PTFE) and SGL 10BB (5% PTFE and MPL). Prior to testing, the test cell was electrochemically activated by repeated cycling between 0.4 V and OCV for 2 h at fully humidified conditions. After activation, the anode side was filled with liquid water. After the flow-field temperature reached target temperature, the cathode side was dry purged for 1 min by 857 sccm air to remove water inside the channel. An image was recorded every minute (i.e., consecutive images of the fuel cell were taken which were each integrated over 1 min) to try to capture water movement. Note that the water reservoir was located 1.2 m above the test cell, indicating the anode side has higher pressure (~12 kPa) than the cathode side, which led to leakage flow from the liquid-filled to dry side under some conditions, described below.

Results and Discussion

Scale analysis of water transport mode in phase-change-induced flow.— A scale analysis and water balance was conducted on a one-dimensional membrane/hydrophobic DM assembly test case shown in Fig. 3 to investigate the major parameters in the phase-change-induced water flow. The model cell consists of the membrane sandwiched between DM, which are in contact with liquid with different temperatures. The assumptions are as follows:

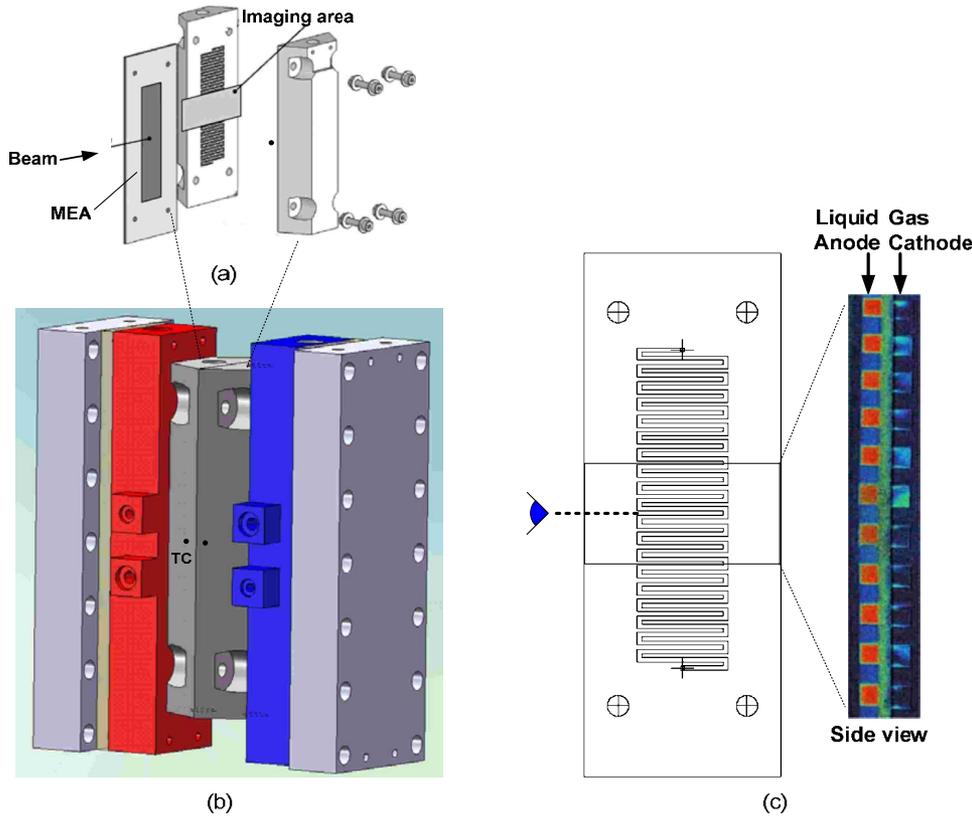1. The local vapor pressure for unsaturated pores is assumed to

Figure 2. (Color online) Schematics of test cell used for neutron radiography: (a) flow-field plate[23], (b) assembled modified test cell with independent coolant plates, and (c) side-on-view for visualization, where the left (anode) side of channels was filled with liquid, and the right (cathode) side was initially purged.

be the saturated vapor pressure at the local temperature. Thus, the gradient of diffusion flux driven by vapor pressure difference in the control volume is net water accumulated by phase change.

2. Heat transfer by the advection is negligible for gas phase and liquid phase. The Peclet number was calculated to be very small to justify this assumption.

An order of magnitude analysis was conducted by considering the following four conservation laws of mass and energy in the porous media as well as membrane.

1. Mass conservation in the porous media

$$\rho_w \varepsilon \frac{\partial s_w}{\partial t} = - \nabla \cdot \vec{J}_{D,v} - \nabla \cdot \vec{J}_c \qquad [1]$$

where ρ_w, ε, s_w, $\vec{J}_{D,v}$, and $\vec{J}_c$, respectively, denote water density, porosity, saturation, vapor diffusion mass flux, and water flux by capillary force. Vapor diffusion mass flux and water flux by capillary action is defined in Eq. 2 and 3
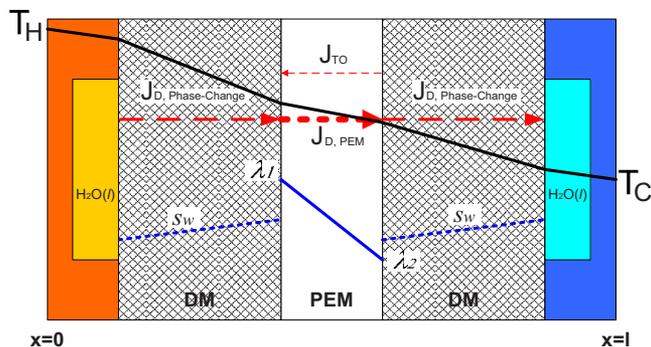

Figure 3. (Color online) Schematic of model cell with membrane and DM assembly set used for scale analysis and thermal model.

$$\vec{J}_{D,v} = - \frac{D_v^{eff}}{R_v} \frac{d\dfrac{P_{sat}(T)}{T}}{dT} \nabla T = - D_{fg} \nabla T \qquad [2]$$

where D_v^{eff}, R_v, P_{sat}, and D_{fg}, respectively, denote effective water vapor diffusivity, vapor gas constant, saturation pressure, and equivalent diffusion coefficient of water vapor in the gas phase resulting from phase-change-induced flow

$$\vec{J}_c = - \rho_w k_{rw} \frac{k_w}{\mu_w} \nabla p_w = - \rho_w k_{rw} \frac{k_w}{\mu_w} \nabla p_c \qquad [3]$$

where k_{rw}, k_w, μ_w, p_w, and p_c, respectively, denote relative water permeability, water permeability, water viscosity, water pressure, and capillary pressure.

2. Mass conservation in the membrane

$$\frac{\rho_{PEM} M_w}{EW} \frac{\partial \lambda}{\partial t} = - \nabla \cdot \vec{J}_{D,PEM} - \nabla \cdot \vec{J}_{TO} \qquad [4]$$

where ρ_{PEM}, M_w, EW, λ, $\vec{J}_{D,PEM}$, and $\vec{J}_{TO}$, respectively, denote density of dry membrane, water molecular weight, equivalent weight of the membrane, water content (the number of water molecules per sulfonic acid site), water diffusion flux, and thermo-osmotic water flux. Water diffusion flux and thermo-osmotic flux in the membrane are defined by Eq. 5 and 6

$$\vec{J}_{D,PEM} = - D_\lambda \frac{M_w \rho_{PEM}}{EW} \nabla \lambda \qquad [5]$$

where D_λ is water diffusivity in the membrane and is a function of water content and temperature

$$\vec{J}_{TO} = - D_{TO} \nabla T \qquad [6]$$

where D_{TO} is thermo-osmotic diffusivity in the membrane and is a function of temperature.[26,27]

3. Energy conservation in the porous media

$$\overline{\rho C_P}\frac{\partial T}{\partial t} = \nabla \cdot k \nabla T + q'''_{\text{gen}} \qquad [7]$$

where $\overline{\rho C_P}$, k, and q'''_{gen}, respectively, denote volume average thermal mass of porous media, thermal conductivity, and heat generation per unit volume. The heat generation per unit volume can be expressed by phase-change term, and the energy equation can be arranged by

$$\overline{\rho C_P}\frac{\partial T}{\partial t} = \nabla \cdot k \nabla T + \nabla \cdot h_{\text{fg}}D_{\text{fg}} \nabla T$$
$$\approx \nabla \cdot \{[k + k_{\text{eqv}}(T)] \nabla T\} = \nabla \cdot [k_{\text{tot}}(T) \nabla T] \quad [8]$$

where h_{fg}, k_{eqv}, and k_{tot}, respectively, denote heat of vaporization per unit mass, conduction equivalent thermal conductivity resulting from phase-change-induced flow, and total thermal conductivity. Note that this energy equation in the porous media was approximated by using equivalent heat conduction thermal conductivity from phase change. Equivalent thermal conductivity, k_{eqv}, is defined as

$$k_{\text{eqv}} \equiv h_{\text{fg}}D_{\text{fg}} = h_{\text{fg}}\frac{D_v^{\text{eff}}}{R_v}\frac{d\dfrac{P_{\text{sat}}(T)}{T}}{dT} \qquad [9]$$

Equivalent thermal conductivity from phase change can be calculated as a function of temperature by using typical tortuosity (τ ~ 1.5), vapor diffusivity relations (Eq. 13 and 14), and $P_{\text{sat}}(T)/T$ relations with temperature. Instead of coupled mass (flow) equation and energy equation, a decoupled energy equation can be used to estimate the temperature distribution.

4. Energy conservation in the membrane

$$\overline{\rho C_P}\frac{\partial T}{\partial t} = \nabla \cdot k \nabla T \qquad [10]$$

where $\overline{\rho C_P}$ and k are the volume average thermal mass and thermal conductivity of membrane, respectively.

Liquid water is filled in both anode and cathode channels and the temperature boundary conditions are

$$T = T_{\text{H}} \quad \text{at} \quad x = 0 \qquad [11]$$

$$T = T_{\text{C}} \quad \text{at} \quad x = l \qquad [12]$$

As shown in Fig. 3, in the hot side (left side of PEM), water vapor condenses inside the DM and on the surface of the membrane, increasing water content of membrane and liquid water saturation in the DM. In the cold side, water in the membrane evaporates and condenses inside the DM or on the flow-field plate surface. Water saturation increase in the pores of the hydrophobic DM increases capillary pressure, driving liquid water toward locations of lower pressure (e.g., larger hydrophobic pores or hydrophilic locations). To estimate the maximum water flux by phase change, the water flux by vapor diffusion in the DM and water flux in the membrane were estimated by Eq. 2, 5, and 6.

From Eq. 2, vapor diffusion flux in the DM is proportional to temperature gradient and equivalent vapor diffusivity. The equivalent vapor diffusivity linearly increases with effective vapor diffusivity and is a function of saturation pressure change with temperature. The vapor diffusivity decreases with liquid saturation and tortuous path in the DM.[19] In this analysis, which estimates the maximum vapor diffusion flux, liquid saturation was assumed to be zero. Thus, the effective diffusivity in the DM can be approximated by[19]

$$D_v^{\text{eff}} = \frac{D_v}{\tau} \qquad [13]$$

where τ is tortuosity. Typical tortuosity in the DM is 1.5. Vapor diffusivity in the air, D_v, is a function of temperature and pressure, expressed by[35]

$$D_v = D_{\text{vo}}\left(\frac{T}{T_o}\right)^n\left(\frac{p_o}{p}\right) \qquad [14]$$

where D_{vo} is the diffusivity at absolute temperature T_o and pressure p_o. D_{vo} is $0.226 \pm 0.003 \times 10^{-4}$ m²/s at 273.15 K and 1 bar, and n is 1.81. Vapor diffusivity increases almost linearly with temperature in the typical PEFC operation ranges (20–80°C). Saturation pressure and the derivative of P_{sat}/T with temperature increase nonlinearly with temperature.

Thus, phase-change-induced flow in the DM can be more important at high temperatures (>50°C) and can be strongly affected by the effective diffusivity. It should be noted that effective vapor diffusivity has some variation and can be affected by saturation and material property (porosity and hydrophobicity) of DM.

To estimate water flux by phase change, the temperature gradient in the DM was estimated by an anisotropic thermal model in the assembly set of R-PEM sandwiched between SGL 10BB DM (compressed thickness 291 μm), discussed in Ref. 27. Total thermal conductivity, sum of conduction equivalent thermal conductivity resulting from phase change (0.33 and 0.6 W/m K for $T_{\text{cell,avg}} = 65$ and 80°C, respectively) and intrinsic material thermal conductivity, was used for this thermal model.[27] In the case of steady state with a cell temperature difference of 10°C and a cell average temperature of 65°C, a 2.9–3°C, <0.5°C, and 1.7–1.8°C temperature drop occurs in each DM, membrane, and each flow field and water inside the channel, respectively.

Figure 4a shows that the estimated water flux by phase change in the DM (SGL 10BB) increases sharply with temperature, indicating that phase-change-induced flow is significant in the high-temperature region and is also strongly affected by the effective diffusivity. For typical effective diffusivity relation expressed by Eq. 13 and at average cell temperature of 65°C, the estimated water flux is ~0.0015 kg/m² s, which is a similar order of magnitude observed in measurement (see Fig. 6). Use of a lower effective diffusivity represents the realistic effect of increased effective tortuosity from liquid saturation.

Water diffusivity in the membrane is dependent on water content, temperature, and materials. Water diffusivity in R-PEM membrane was observed to be ~50% of that in Nafion membrane.[36] Diffusivity does not change significantly for water content (λ) between 8 and 19, where ionic conductivity does not change significantly. Water diffusivities of N112 and R-PEM membranes can be approximately 2.87×10^{-10} and 1.44×10^{-10} m²/s, respectively, for water content between 8 and 19.[36] Figure 4b shows estimated diffusion water flux in both membranes at average temperature of 65°C as well as estimated net water flux, which is a sum of thermo-osmosis and mass diffusion water flux. Thermo-osmotic water flux is from the cold to the hot side, the opposite direction to mass diffusion. Thermo-osmotic water flux was estimated by empirical relations,[26,27] and is 0.00024 and 0.00041 kg/m² s for Nafion 112 and R-PEM membranes, respectively.

Diffusion water flux in the membrane and phase-change-induced water flux in the DM have a similar order of magnitude. In normal situations, it appears neither mode is dominant and both modes contribute to the net water flux, because there are some variations in the effective vapor diffusivity with saturation (s_w) in the DM and CL as well as water diffusivity with water content (λ) in the membrane. However, the effective vapor diffusivity, membrane diffusivity, average cell temperature, and temperature gradient play an important role in parameters in the phase-change flow. Water flux can be engineered by tailoring thermal and material properties to suit the desired conditions.

Direct experimental measurement.— Figure 5 shows measured water flux through the Nafion membrane without a CL sandwiched between hydrophobic DM (SGL10BB) or hydrophilic DM (SGL10AA). The net water flux in the assembly with hydrophobic DM and membrane was proportional to the temperature difference, and the flux amount increased with cell average temperature, as in
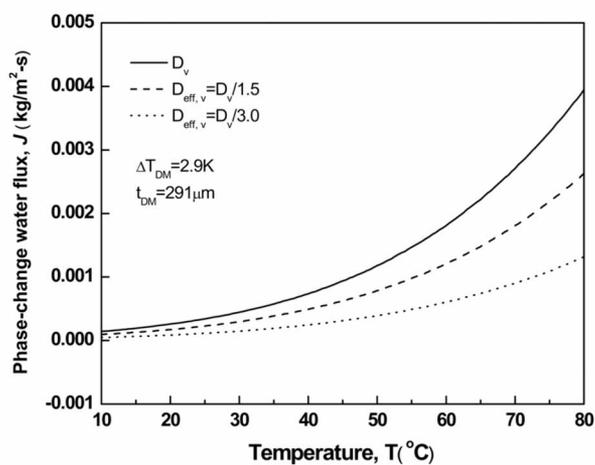
(a) Vapor flux through diffusion media
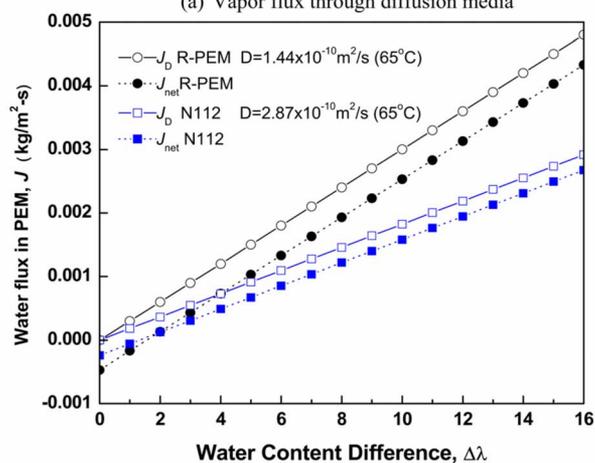
(b) Calculated diffusion and net water flux through membrane at average cell temperature of 65°C.

Figure 4. (Color online) Estimated water flux due to phase change with different vapor diffusivity through DM and water flux in the membrane due to concentration gradient.

the hydrophilic DM and membrane assembly. However, the net water flux direction was instead from the hot to cold direction and the amount of water flux increased by nearly 7 times compared to that of the completely liquid saturated hydrophilic DM and membrane assembly case. It should be noted that the negative value of water flux was chosen arbitrarily and represents water flow from the cold to the hot side.

For cases with hydrophobic DM, some gas-phase saturation in the MPL of SGL10BB contact with membrane exists due to very high capillary pressure, even when the water was filled with a vacuum. Kim and Mench[26,27] observed negligible water flux through fully saturated hydrophilic DM (SGL10AA) under temperature gradient and water flow from cold to hot in the Nafion 112 membrane. Contrary to hydrophilic DM, in the hydrophobic DM (SGL 10BB), water can evaporate at the higher temperature side, diffuse through unsaturated void volume, and condense on the cold side of the unsaturated pore. For hydrophobic DM and membrane assembly cases, the water transport mode by phase-change-induced flow dominates compared to thermo-osmosis in the membrane, which is in the opposite direction.

The reinforced membrane (R-PEM) without CL was also observed to have similar behavior. Figure 6 shows water flux of R-PEM at 45 and 65°C. Surrounded by hydrophilic DM, water flux of R-PEM was almost twice that of Nafion 112 membrane at 45 and 65°C. However, sandwiched by hydrophobic DM (SGL 10BB), the
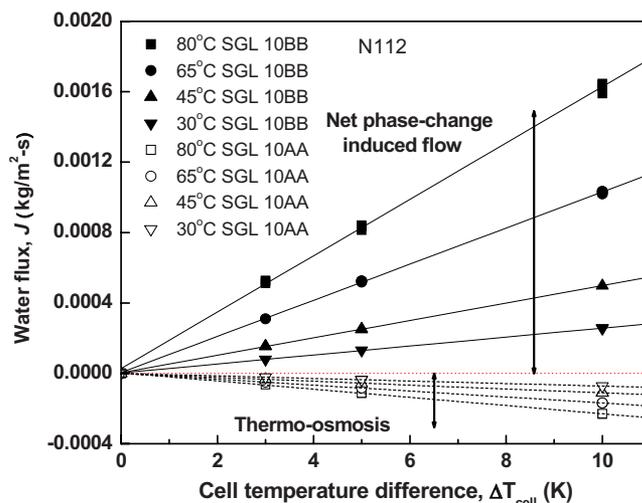

Figure 5. (Color online) Effect of hydrophobicity of DM on temperature-driven water flux through Nafion 112 membrane at various average cell temperatures.

R-PEM had only 8.5 and 23.5% higher water flux than a similarly situated N112 membrane at 45 and 65°C, respectively. Even if R-PEM has higher thermo-osmotic water flux to the hot side compared to N112, the overall net water flux by phase change was observed to be higher toward the cold side for the R-PEM case. This is because the temperature difference across the membrane is small (~ 0.4°C), leading to small thermo-osmosis, and the diffusion flux in the membrane is nonlimiting and high because of significant phase-change-induced flow in the DM. As shown in Fig. 4b, assuming the same vapor-phase water flux in the DM in both R-PEM and N112 membrane cases, diffusion flux in the membrane is dominant, and the R-PEM has a higher diffusion flux.

The effect of existence of CLs, hydrophobicity of DM, MPL, and nonreinforcement of membrane on water flux was summarized in Table III. The existence of a CL also results in gas-phase voids, and a net phase-change-induced water flux direction toward the cold side, even if the hydrophilic DM (SGL10AA) were used to sandwich the three-layer MEA. As seen in the activation plot (Fig. 8), the slope was similar to other hydrophobic DM cases, indicating water transport mode is dominated by the phase-change-induced flow in
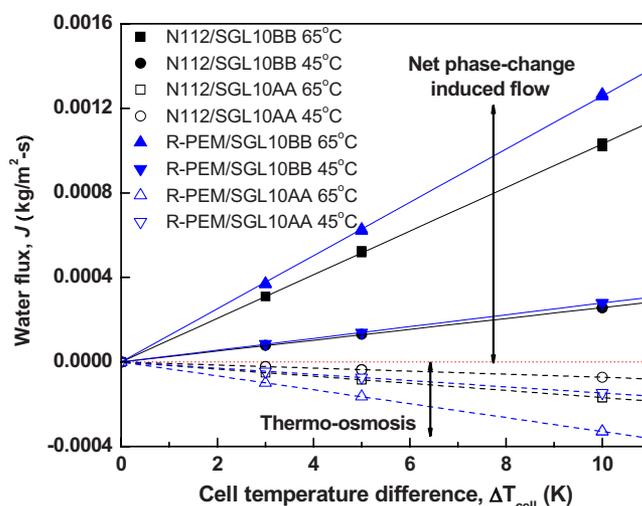

Figure 6. (Color online) Comparison of reinforced membrane (R-PEM, 18 μm) and nonreinforced (Nafion 112) membranes with different hydrophobic DM at average cell temperatures of 65 and 45°C.

Table III. Comparison of temperature-driven flow at average cell temperature of 65°C in different combination of MEAs and DM.

PME/MEA	DM	Water flux, J (kg/m² s)
R-PEM (Gore-Select 18 μm thick)	SGL 10AA	$J = -3.502 \times 10^{-5} \, \Delta T_{cell}$
R-MEA (Gore Primea 5710 series)	SGL 10AA	$J = 4.351 \times 10^{-5} \, \Delta T_{cell}$
R-MEA (Gore Primea 5710 series)	SGL 10BA	$J = 7.311 \times 10^{-5} \, \Delta T_{cell}$
R-MEA (Gore Primea 5710 series)	SGL 10BB	$J = 1.486 \times 10^{-4} \, \Delta T_{cell}$
NR-MEA	SGL 10AA	$J = 5.658 \times 10^{-5} \, \Delta T_{cell}$
NR-MEA	SGL 10BB	$J = 1.659 \times 10^{-4} \, \Delta T_{cell}$

these situations. The mixed wettability in the CLs creates a gas-phase boundary between membrane and porous media (CL). However, the phase-change-induced flow was significantly lower than hydrophobic DM (SGL10BB) with a bare membrane. This is explained by a result of the low effective vapor diffusivity (due to postulated low unsaturated void volume) in the CL and very thin profile with low temperature gradient to induce flow. Nevertheless, it is interesting to see that even the CL contributes to net flow, despite its thickness and should not be ignored in analysis.

From Table III, effect of extent of hydrophobicity on water transport rate shows that water flows from hot to cold side for all cases with hydrophobicity attributable to CLs or DM. From the comparison of water flux in the SGL10BB and 10BA (no MPL) test cases, the MPL layer was observed to have a significant role in water transport rate under temperature gradient. Hydrophobic DM increased water transport rate significantly compared to the three-layer MEA with hydrophilic DM. There is a phase-change-induced flow across the gas voids in the CL, MPL, and main DM. Overall, the water transport was dominated by the phase-change-induced flow in the DM. The difference of water transport rate can be attributed to the availability of void space in the porous media and temperature gradient. SGL 10BB is made by coating mixture of carbon black and PTFE on the one side of SGL 10BA. The MPL thickness is approximately 60–80 μm and 23% PTFE content and small pore size, resulting in very high capillary pressure and very low liquid saturation compared to 5% PTFE-coated SGL10BA.[12] The MPL layer has very low liquid saturation and high void space for water vapor diffusion, resulting in a higher water vapor diffusion rate. Higher water satu-
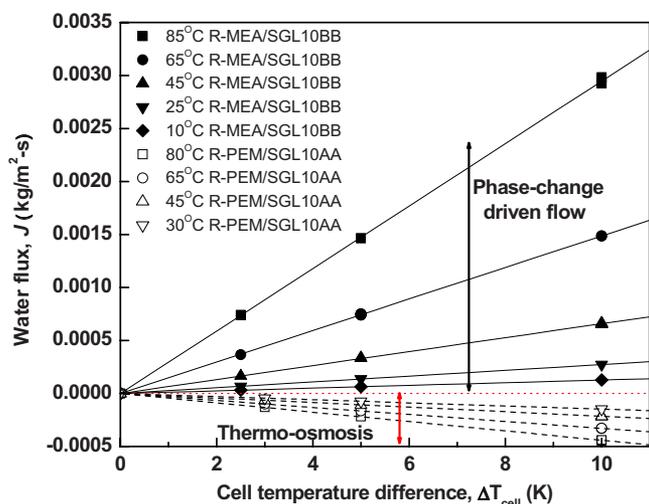

Figure 7. (Color online) Effect of DM (with MPL) and CL on temperature-driven water transport in R-MEA at different temperatures.
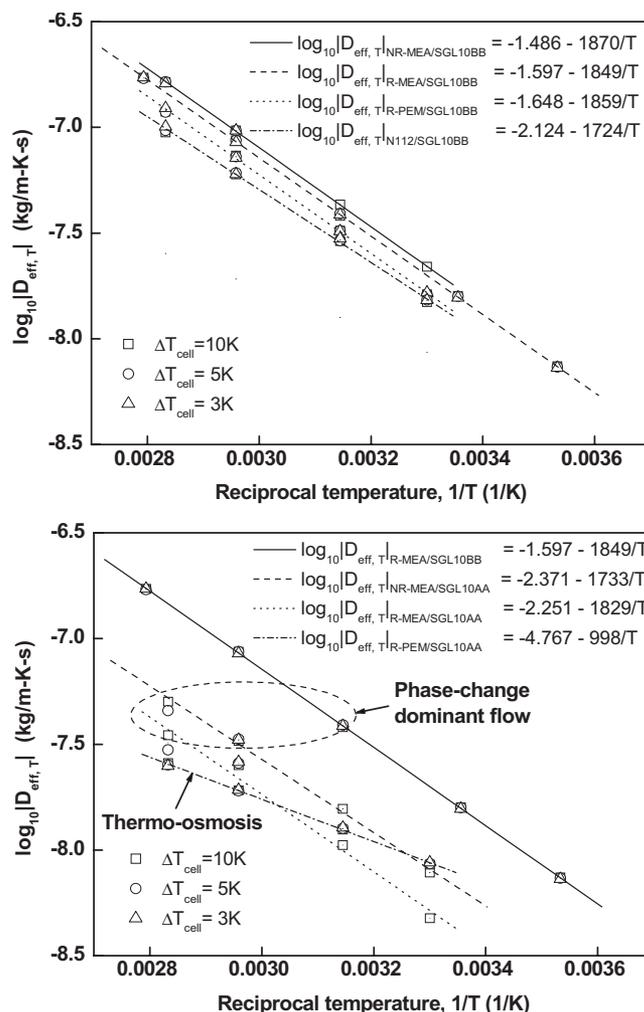
Figure 8. Comparison of phase-change driven flow and thermo-osmotic diffusivity of different materials.

ration in the DM SGL 10BA can reduce effective water vapor diffusivity, leading to decreasing water flux. It was also observed that water flux in the MEA with SGL10AA case had the highest water flux when MEA and DM are in a dry state at the initial condition. However, as time elapsed, the water flux to the cold side decreased to the steady value as water saturation in the DM (SGL10AA) increased.

From Table III, the MEA with nonreinforced membrane was observed to have slightly higher net water flux with both hydrophilic and hydrophobic DM than the reinforced membrane. It is expected that the nonreinforced membrane has higher water diffusivity than the reinforced membrane because the nonreinforced membrane has higher water passage than the reinforced part. From this observation, net water flux can be affected by diffusion mode in the membrane and the vapor diffusion rate in the unsaturated pores. It should be noted that CLs and ionomers in the membrane are identical for both types of MEA.

Figure 7 shows the temperature-driven water flux of R-MEA sandwiched between two SGL10BB DM, which is a typical combination of fuel cell. Within the measured temperature ranges, water flows from the hot to the cold side, as a result of phase-change-induced flow across the unsaturated regions of the CL, MPL, and DM, and shows linear relationships with temperature difference.

Figure 8 shows plots of the effective temperature-driven mass diffusivity ($D_{\mathrm{eff},T}$), defined as water flux per temperature gradient $[|\vec{J}_T|/dT/dx]$ vs reciprocal of average cell temperature. Test data for
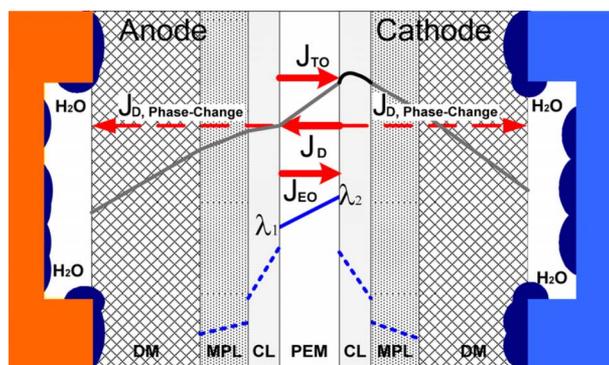
(a) During operation or center cells after shutdown
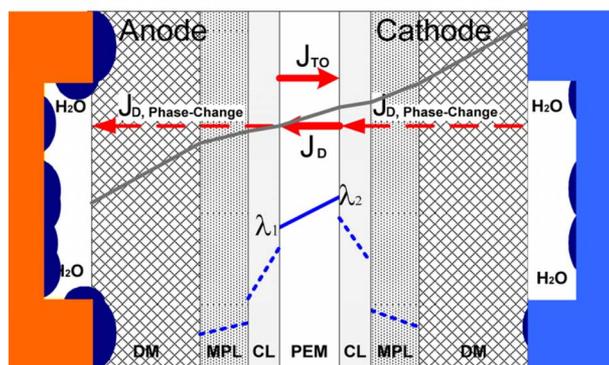
(b) Anode end cell after shutdown

Figure 9. (Color online) Schematic of water transport modes of fuel cell.

a particular material set were collapsed into a single line on the log scale plot, and the slope is constant, which can be considered as activation energy in an Arrhenius rate law expression. Arrhenius rate expressions for different material sets (thermo-osmosis and phase-change dominant-induced flow) are also shown in Fig. 8. Test cases with hydrophobicity ascribed to CL or DM were observed to have similar activation energy and to be less sensitive to materials, MEA or membrane. However, between thermo-osmotic and phase-change-induced flow, the slope (e.g., activation energy) was significantly different, indicating that the fundamental transport mechanism is different between the two modes of temperature-driven transport. Phase-change-induced flow is a net flow of thermo-osmosis and diffusion in the membrane, vapor diffusion in the porous media, and phase change in the porous media or interfaces.

If any gas phase and liquid water coexist in the fuel cell materials (typically in DM, CL, or MPL) and there is a temperature gradient, water transports by phase-change-induced flow through porous media. This is a normal case for fuel cell operation. Figure 9a shows schematic water transport modes and water distribution of actual fuel cell operation. The cathode CL is hottest and flow-field plates

are colder, inducing phase-change flow toward flow-field plates through the porous media (water can also transport by capillary flow). In the membrane, thermo-osmotic and electro-osmotic water flows from the anode to cathode, contrary in most cases to diffusion flux. Thermo-osmotic water flux is proportional to temperature gradient, and for Gore-Select (18 μm thick) membrane thermo-osmotic water flux is equivalent to product water at 400 mA/cm^2 for the membrane temperature difference of 0.3°C.[27] At high current operation, thermo-osmotic water flux can be more important because membrane temperature difference may be over 1°C. The importance of thermo-osmotic water transport is also strongly dependent on membrane water diffusivity.[27] A schematic temperature distribution shown in Fig. 9a can be applied to all cells in a fuel cell stack, while coolant is circulated through all flow-field plates. During the shutdown, center cells in the fuel cell stack also have similar temperature profile shown in Fig. 9a, but the anode and cathode end cells have heat flow toward the end plate as shown in Fig. 9b. In the anode end cell, liquid water can accumulate in the cathode CLs, resulting in damage in the frozen condition.[31,32]

For this direct measurement of water flux (simulated phase-change-induced flow testing), both anode and cathode channels were fully saturated with liquid water and the DM had some saturation ($\approx$1 for untreated SGL 10AA case), as shown in the schematic diagram of Fig. 3. In this experimental setup applying a temperature difference across the cell, most of the temperature drop occurs in the DM, based on the analysis of two-dimensional anisotropic thermal model.[27] For example, for 10°C cell temperature difference, the temperature difference across the membrane was computed to be <0.5°C (0.47 and 0.4°C for $T_{cell,avg}$ = 80 and 65°C, respectively), resulting in water flux (<0.0007 kg/m^2 s) in the hot direction.[26,27] This flux amount is 30% of the measured net flux (hot to cold direction). Thus, mass diffusion in the membrane is dominant compared to thermo-osmosis.

The differences between this simulated phase-change-induced flow testing and actual fuel cells are described in Table IV. Although infinite heat and water source (energy and mass source for evaporation) and heat sink are used in experiment, the heat source (heat generation by current) and heat sink (cooling) are finite in real fuel cells. Thus, water transport by phase-change-induced flow in the real application is more important in high current operation because of the available heat source. Additionally, in the high current operation, the temperature difference in the membrane can also be >1°C,[16,17] driving water from the anode (cold) to the cathode (hot) side via thermo-osmosis. This corresponds to an equivalent water production at ~1.1 A/cm^2.[27] In addition to transported water to the cathode side via electro-osmotic drag, thermo-osmosis can significantly increase water amount in the cathode side. However, higher temperature at the cathode can significantly enhance water removal away from the cathode through the DM via phase-change-induced flow. Note that thermo-osmotic water flux can be significantly reduced due to insufficient liquid water in the anode side, and higher water content in the cathode side can also enhance the back-diffusion. In total, thermo-osmosis, electro-osmosis, back-diffusion, and phase-change-induced flow should be considered for water balance in fuel cell. Thermo-osmosis and phase-change-induced flow can also be important at localized high current regions because of a high tem-

Table IV. Differences between simulated phase-change-induced flow testing and real fuel cell.

| Simulated phase-change-induced flow testing	Real fuel cell testing
Infinite heat source (constant temperature boundary, T_H)	Finite heat source (fuel cell operation) and finite heat sink
Infinite heat sink (constant temperature boundary, T_C)	
$\Delta T_{PEM} < 0.5$°C (for 10°C cell difference)	$\Delta T_{PEM} > 1$–2°C (at 1 A/cm^2 operation or localized high current regions)
Phase-change-induced flow is dominant	Thermo-osmotic water flux can become more important, depending on mass diffusivity
(~30% of net flux may come from thermo-osmosis)	
Thermo-osmosis and diffusion modes in the membrane	Thermo-osmosis, diffusion, and electro-osmosis modes in the membrane
Phase-change-induced flow in DM	Phase-change-induced flow in DM
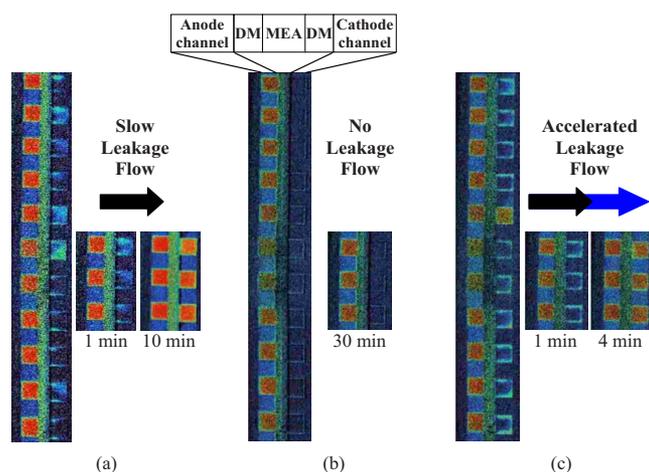
Figure 10. (Color online) Visualized water transport behavior of MEA with hydrophilic DM test set under different temperature gradients: (a) anode/cathode = 65°C/65°C, (b) anode/cathode = 60°C/70°C, and (c) anode/cathode = 70°C/60°C.

Figure 11. (Color online) Visualized water transport behavior of MEA with hydrophobic DM test set under different temperature gradients: (a) anode/cathode = 45°C/45°C, (b) anode/cathode = 40°C/50°C, and (c) anode/cathode = 50°C/40°C.

perature gradient resulting from local ohmic heating. Note that phase-change-induced flow may not occur under dry or low-humidity operation because of lack of available liquid water.

Temperature-driven flow can be very important in the initial stage of shutdown because of high average cell temperature as well as high temperature difference in the membrane. As time elapses during the shutdown, thermo-osmotic water flux is reduced to negligible levels. In this case, the phase-change-induced flow becomes the major water transport mode. However, phase-change-induced flow also decreases with decreasing temperature because saturation pressure is significantly reduced with temperature, especially below 50°C.

Experimental visualization.— Neutron images were taken every minute for 30 min under conditions of different temperature gradients and material sets. Two main material sets were used: a R-MEA with a non-PTFE–treated gas diffusion layer (SGL10AA) with no MPL on the anode and cathode sides, and a diffusion layer set with 5% PTFE and a highly hydrophobic MPL. For cases with the non-PTFE DM set, tests with negligible temperature gradient ($\approx$0°C) revealed a slow leakage of water from the liquid to gas sides (see Fig. 10) via the static pressure head of liquid in the channel, as well as capillary wicking. When the liquid side was colder, however, the phase-change-induced flow reversed and prevented the leakage. When the gas-phase side was colder, the flow from hot to cold was augmented by the phase-change-induced flow and the gas-phase side filled much more quickly.

When the DM were switched to a hydrophobic set with MPL, the breakthrough pressure of the DM was increased, and the gravity-induced leakage of water from the anode to cathode side under a negligible temperature gradient ($\approx$0°C) condition was completely prevented (Fig. 11). However, when the initially gas-phase side of the cell was colder, the channels were filled very quickly by the phase-change-induced flow. In all cases in which the gas side of the assembly was colder, phase-change-induced flow dominated and the net flux was to the cold side.

The modes of temperature-driven transport in PEFCs can be summarized in Table V. In the pure membrane only, flow is driven from the cold to hot locations. In the porous media with incomplete liquid saturation, the phase-change-induced flow is dominant, even for very small temperature gradients and thicknesses. Under high current operation as well as the initial stage of shutdown, thermo-osmosis in the membrane should not be neglected. However, at low
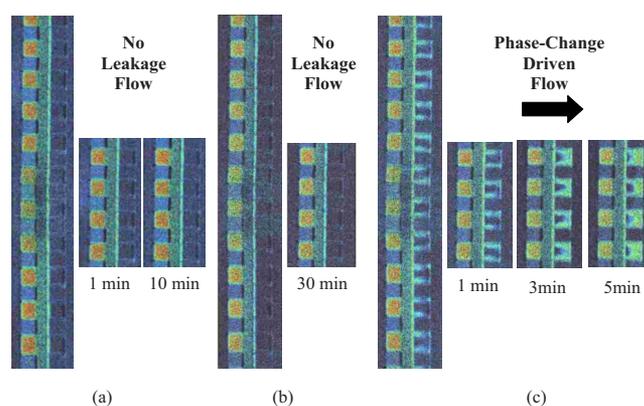
current as well as most of shutdown periods, thermo-osmotic flux in the membrane can be neglected and phase-change-induced flow is dominant.

Conclusions

Temperature-dependent flow in PEFCs was identified to occur in two primary modes: (*i*) Thermo-osmosis in the pure membrane only and (*ii*) phase-change-induced flow, which occurs when there is any gas phase and a temperature gradient in the CL, MPL, or main DM. Both modes are precisely and conveniently fit by Arrhenius expressions with different activation energy, indicating water transport under the phase-change-induced mode is fundamentally different than the thermo-osmotic flow in membranes. Although the slope was not affected, the absolute value of the phase-change-induced flow was affected by average membrane temperature, temperature gradient, and porous media properties.

Gas-phase saturation is a key controlling parameter to determine the water transport mechanism driven by temperature gradient. If some gas phase exists in the CL, MPL, and DM, the phase-change-induced water transport was dominant, and the net water flux was observed from the hot to cold side. The existence of CLs and PTFE-coated DM results in incomplete liquid saturation in the fuel cell porous media. In this normal operating case (incomplete saturation), the phase-change-induced water transport mode is dominant. Neutron radiography confirmed and visualized the phase-change-induced water flow from hot to cold locations in PEFCs with incomplete saturation of porous media.

Thermo-osmotic water transport, showing water flux on the cold to the hot direction, can be more important when fuel cell is operated in the high current as well as initial stage of shutdown. The importance of thermo-osmotic water transport is strongly dependent on membrane water diffusivity.

Water balance in fuel cells can be engineered by controlling thermal and material properties. Incorporation of thermo-osmosis and evaporative flow into modeling is critical to ensure accurate results.

Table V. Differences between thermo-osmosis and phase-change-induced flow.

Transport mode	Thermo-osmosis	Phase-change-induced flow (heat pipe flow)
Materials	Membrane	Porous media (CL or DM)
Driving force	Entropy change between liquid out of membrane and in membrane	Gradient of saturation pressure with temperature
Flux direction	Hot-to-cold or cold-to-hot direction, depending on membrane properties; for a hydrophilic membrane flow is from cold to hot side	Always hot-to-cold direction
Schematic		
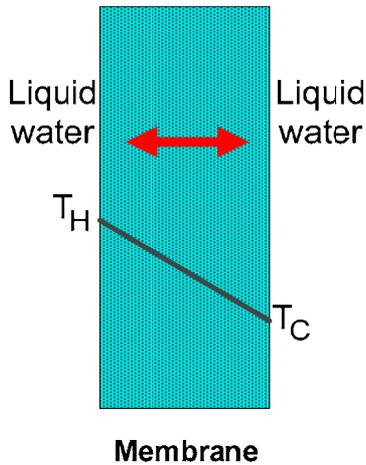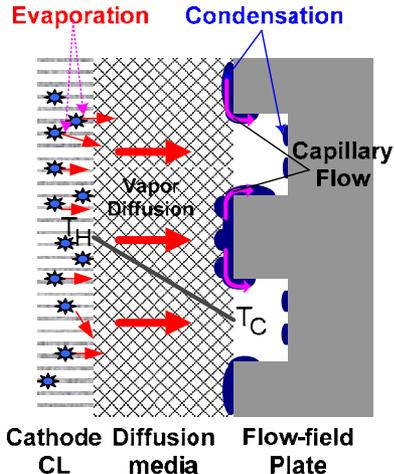
List of Symbols

C_p	specific heat capacity, J/kg-K
h_{fg}	enthalpy of melting per unit mass, J/kg
J	water flux, kg/m^2-s
D	diffusivity, m^2/s
k	thermal conductivity, w/m-K
k_{rw}	relative permeability of water
k_w	permeability of water, m^2
M	molecular weight, kg/kmol
R_v	vapor gas constant, 0.4615 kPa-m^3/kg-K
T	temperature, K
TC	thermocouple

Subscripts

C	cold
D	diffusion
C	capillary flow
fg	phase change from liquid to gas
H	hot
sat	saturation
w	liquid phase water
v	vapor phase water
eq	equivalent

Superscripts

eff	effective

Greek

λ	membrane water content
ρ	density, kg/m^3

References

1. S. Kim and M. M. Mench, *J. Power Sources*, **174**, 206 (2007).
2. S. Kim, B. K. Ahn, and M. M. Mench, *J. Power Sources*, **179**, 140 (2008).
3. G. J. M. Janssen, *J. Electrochem. Soc.*, **148**, A1313 (2001).
4. T. F. Fuller and J. Newman, *J. Electrochem. Soc.*, **140**, 1218 (1993).
5. M. Eikerling, Y. I. Kharkats, A. A. Kornyshev, and Y. M. Volfkovich, *J. Electrochem. Soc.*, **145**, 2684 (1998).
6. S. Ge, X. Li, B. Yi, and I. Hsing, *J. Electrochem. Soc.*, **152**, A1149 (2005).
7. A. Z. Weber and J. Newman, *J. Electrochem. Soc.*, **151**, A326 (2004).
8. A. Z. Weber and J. Newman, *J. Electrochem. Soc.*, **151**, A311 (2004).
9. G. J. Janssen and M. L. Overvelde, *J. Power Sources*, **101**, 117 (2001).
10. X. Ren and S. Gottesfeld, *J. Electrochem. Soc.*, **148**, A87 (2001).
11. S. Ge, B. Yi, and P. Ming, *J. Electrochem. Soc.*, **153**, A1443 (2006).
12. E. C. Kumbur, K. V. Sharp, and M. M. Mench, *J. Electrochem. Soc.*, **154**, B1315 (2007).
13. J. T. Gostick, M. W. Fowler, M. A. Ioannidis, M. D. Pritzker, Y. M. Volfkovich, and A. Sakars, *J. Power Sources*, **156**, 375 (2006).
14. S. Litster, D. Sinton, and N. Djilali, *J. Power Sources*, **154**, 95 (2006).
15. Q. Ye and T. V. Nguyen, *J. Electrochem. Soc.*, **154**, B1242 (2007).
16. M. Khandelwal and M. M. Mench, *J. Power Sources*, **161**, 1106 (2006).
17. A. Z. Weber and J. Newman, *J. Electrochem. Soc.*, **153**, A2205 (2006).
18. R. Bradean, H. Haas, K. Eggen, C. Richards, and T. Vrba, *ECS Trans.*, **3**(1), 1159 (2006).
19. M. M. Mench, *Fuel Cell Engines*, Chap. 5, John Wiley & Sons, Hoboken, NJ (2008).
20. Y. Wang and C. Y. Wang, *J. Electrochem. Soc.*, **153**, A1193 (2006).
21. M. A. Hickner, N. P. Siegel, K. S. Chen, D. N. McBrayer, D. S. Hussey, D. L. Jacobson, and M. Arif, *J. Electrochem. Soc.*, **153**, A902 (2006).
22. M. A. Hickner, N. P. Siegel, K. S. Chen, D. S. Hussey, D. L. Jacobson, and M. Arif, *J. Electrochem. Soc.*, **155**, B294 (2008).
23. M. A. Hickner, N. P. Siegel, K. S. Chen, D. S. Hussey, D. L. Jacobson, and M. Arif, *J. Electrochem. Soc.*, **155**, B427 (2008).
24. M. Tasaka, T. Mizuta, and O. Sekiguchi, *J. Membr. Sci.*, **54**, 191 (1990).
25. M. Tasaka, T. Hirai, R. Kiyono, and T. Aki, *J. Membr. Sci.*, **71**, 151 (1992).
26. S. Kim and M. M. Mench, *ECS Trans.*, **13**(28), 89 (2008).
27. S. Kim and M. M. Mench, *J. Membr. Sci.*, In press. [DOI: 10.1016/j.memsci.2008.11.043]
28. J. P. G. Villaluenga, B. Seoane, V. M. Barragan, and C. Ruiz-Bauza, *J. Membr. Sci.*, **274**, 116 (2006).
29. R. Zaffou, J. S. Yi, H. R. Kunz, and J. M. Fenton, *Electrochem. Solid-State Lett.*, **9**, A418 (2006).
30. R. Zaffou, H. R. Kunz, and J. M. Fenton, *ECS Trans.*, **3**(1), 909 (2006).
31. M. Perry, T. Patterson, and J. O'Neill, *2007 U.S. DOE Annual Program Review Proceedings*, DOE, Washington (2007), http://www.eere.energy.gov
32. M. Perry, T. Patterson, and J. O'Neill, *Proc. of 5th International Conference on Fuel Cell Science Engineering and Technology*, New York, June 18–20, Paper no. ASME FUELCELL2007-25338, ASME, New York (2007).
33. S. Cleghorn, J. Kolde, and W. Liu, in *Handbook of Fuel Cells, Fundamentals, Technology and Applications*, W. Vielstich, H. A. Gasteiger, and A. Lamm, Editors, pp. 566–575, John Wiley & Sons, Hoboken, NJ (2003).
34. SIGRACET GDL 10 Series Gas Diffusion Layer Property Sheet, SGL TECHNOLOGIES GmbH (2004).
35. R. B. Montgomery, *J. Meteorol.*, **4**, 193 (1947).
36. X. Ye and C. Y. Wang, *J. Electrochem. Soc.*, **154**, B676 (2007).